High-efficient and Comprehensive Modeling of MFIM Ferroelectric Tunnel Junctions for Non-volatile/Volatile Applications

Yu Li[1], Hao Jiang[1,2,*], Jie Yu[1], Xuanyu Zhao[1], Xiaodong Wang[1], Qihan Liu[1], Yingfen Wei[1,2,*], Qi Liu[1,2,*], and Ming Liu[1,2]
[1]State Key Laboratory of Integrated Chips and Systems, Frontier Institute of Chip and System, Fudan University, Shanghai, 200433, China; [2]Zhangjiang Fudan International Innovation Center, Fudan University, Shanghai 200433, China.
[*]Email: haoj@fudan.edu.cn; yingfen_wei@fudan.edu.cn; qi_liu@fudan.edu.cn.

***Abstract*—In this work, we demonstrate an efficient and comprehensive model for designing non-volatile and volatile ferroelectric tunnel junctions (FTJs), based on Metal-Ferroelectric-Insulator-Metal (MFIM) structure. 1) A high-efficient dynamic module is developed to simulate polarization retention loss and capture the multi-domain reversal by involving an inhomogeneous field distribution. 2) The potential profile calculation involves the contributions of screening charge and image force, which play significant roles in the depolarization field, ON-state current density (J_{ON}), and tunneling electroresistance (TER) ratio. 3) The design spaces of material properties to optimize the non-volatile/volatile performance are systematically investigated, enriching the capability of MFIM FTJs.**

Keywords*—Ferroelectric tunnel junction (FTJ), Hafnia-based ferroelectric materials, polarization retention loss.

I. Introduction

Hafnia-based ferroelectric tunnel junctions (FTJs) have been suggested as one of the most promising candidates for emerging memory and computing technologies, thanks to their non-destructive readout, low power consumption, and CMOS and BEOL compatibility [1]. Among all the reported FTJ structures, the Metal-Ferroelectric-Insulator-Metal (MFIM) one features a high endurance, excellent linearity of conductance modulations, and friendly 3D stackability [2].

FTJs exhibit either nonvolatile or volatile behavior, depending on the device stacks and the resulting depolarization field applied to the ferroelectric (FE) layer [3]. A powerful FTJ model with more comprehensive physical mechanisms that can accurately capture the dynamics responses to depolarization, while maintaining computational efficiency, is essential for guiding device engineering to meet specific requirements of non-volatile (e.g., storage memory and neuromorphic synaptic device) and volatile (e.g., artificial neuron and reservoir computing) applications (Fig. 1(a)).

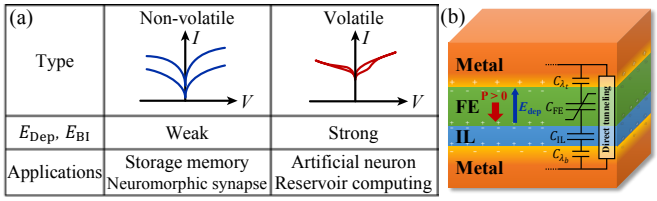

Fig. 1. (a) Proposed non-volatile and volatile applications based on FTJ devices, determined by the strength of depolarization field and built-in field. (b) Schematic of an MFIM FTJ device. The equivalent circuit is illustrated on the right side.

In this work, we present our efforts to develop such a high-efficient and comprehensive FTJ model based on an MFIM structure (Fig. 1(b)). Compared with the previously reported FTJ models [4–8], *i*) the multi-domain characteristics of polycrystalline HfO_2 FE films are modeled in a more efficient manner, by parameterizing the inhomogeneous mechanism into a partial differential equation (PDE), accurately capturing the polarization reversal dynamics; *ii*) the potential profile is calculated by a more thorough physical model including both the screening charge (SC) and image force (IF) effects; *iii*) for the first time, the dynamic retention behaviors and their dependence on key material parameters are systematically studied and discussed, in addition to the modeling of ON-state current density (J_{ON}) and the tunneling electroresistance (TER) ratio, which are crucial for both non-volatile and volatile applications.

II. Simulation Framework

Fig. 2 illustrates the flowchart framework and theoretical formalism of our MFIM FTJ model. During the polarization reversal, the electric field on the FE layer (E_{FE}) is calculated

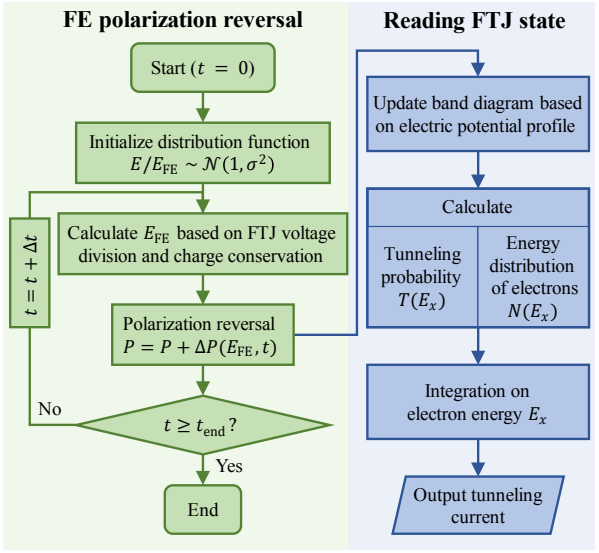

Polarization reversal	Current-voltage characteristics
Voltage division of FTJ device $V_{app} + V_{BI} = V_m + E_{FE}t_{FE} + E_{IL}t_{IL}$ Screening charge in metal: $V_m = \rho_s\lambda_m/\epsilon_m$ Built-in field: $V_{BI} = (\Phi_t + \Phi_c - \Phi_b)/e$ **Continuity of electric charge at interfaces** $\rho_s = P_{FE} + \epsilon_{FE}E_{FE} = \epsilon_{IL}E_{IL} = \epsilon_m E_m$ ⇒ **Electric field in FE layer** $E_{FE} = \frac{V_{app} + V_{BI} - P_{FE}(\sum \lambda_m/\epsilon_m + t_{IL}/\epsilon_{IL})}{t_{FE} + \epsilon_{FE}(\sum \lambda_m/\epsilon_m + t_{IL}/\epsilon_{IL})}$ **Dynamic reversal of FE polarization** Normal distribution of local E-field $X(E/E_{FE}) \sim \mathcal{N}(1,\sigma^2)$ Empirical Merz's law of switching time $\tau(E) = \tau_0 \exp[(E_a/E)^\alpha]$ Reversal event determined by step function $p(t,E) = \begin{cases} 2P_r, & t \geq \tau(E) \\ 0, & t < \tau(E) \end{cases}$ Total polarization reversal $\Delta P(t, E_{FE}) = \int_0^\infty dE\, X(E/E_{FE})\, p(t,E)$ Time-dependent PDE for reversal dynamics $\frac{\partial P}{\partial t} = \frac{2P_r}{\sqrt{\pi}} \frac{E_a}{E_{FE}\sqrt{2}\sigma} \exp\left\{-\left[\frac{E_a}{E_{FE}\ln(t/\tau_0)^{1/\alpha}\sqrt{2}\sigma}\right]^2\right\} \cdot \frac{1}{\alpha t \ln^2(t/\tau_0)^{1/\alpha}}$	**Electrostatic potential profile** (1) Basic tunnel barrier Trapezoidal potential in FE, IL $U_0(x) = \Phi_1 + (\Phi_2 - \Phi_1 - eV_i)x/d$ (2) Modulations Screening charge potential in metal $U_{SC}(x) = \pm\frac{\rho_s\lambda_m \exp(-\lvert x\rvert/\lambda_m)}{\epsilon_m}$ Image force potential in FE, IL $U_{IF}(x) = \frac{e^2}{8\pi\epsilon}\sum_0^\infty (k_1k_2)^n \left(\frac{k_1}{x+nd} + \frac{k_2}{(d-x)+nd} + \frac{2k_1k_2}{d+nd}\right)$ with $k_i = \frac{\epsilon-\epsilon_i}{\epsilon+\epsilon_i}(i = 1,2)$ 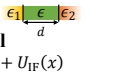 **Effective tunneling potential** $U(x) = U_0(x) + U_{SC}(x) + U_{IF}(x)$ **Tunneling current (WKB approx.)** Tunneling probability $T(E_x) = \exp\left[-\frac{4\pi}{h}\int_0^d \sqrt{2m_{eff}[eU(x) - E_x]}\,dx\right]$ Energy distribution of electron $N(E_x) = k_BT \cdot \ln\left[\frac{1+\exp\left(\frac{E_{F2}-E_x}{k_BT}\right)}{1+\exp\left(\frac{E_{F1}-E_x}{k_BT}\right)}\right]$ Direct tunneling current $J = \frac{4\pi m_{eff}e}{h^3}\int_{E_{min}}^{E_{max}} T(E_x)\, N(E_x)\, dE_x$

Fig. 2. (a) Framework of our MFIM FTJ model, including the time-dependent polarization reversal (green), and current-voltage characteristics during the Read operation (blue). (b) Critical equations used in our MFIM FTJ model, including modules to calculate ferroelectric polarization dynamics and electric transport property. Left column: the polarization reversal dynamics is calculated by solving a single PDE where the inhomogeneous field on multi-domains is parameterized by the deviation σ. Right column: tunneling current is calculated based on WKB approximation, with the tunnel barrier modulated by the screening charge and image force effects.

based on the voltage drop across layers and the continuity of electric charge at interfaces.

In addition, the inhomogeneous local electric field is applied on each FE domain in a polycrystalline FE thin film, which is assumed to be a Gaussian distribution [9]. The inhomogeneous field mechanism (IFM) is associated with a widespread characteristic switching time. Furthermore, inspired by the cumulative function of polarization reversal, we derive a time-dependent PDE to describe the collective effect of reversal events. Direct tunneling mechanism based on the well-known WKB model [4, 6–8, 10] is used to simulate the read current of FTJ at different polarization states, with considerations of SC potentials [5, 8, 11] of metal electrodes and IF potentials [10] of FE and IL layers in our work.

III. Polarization Reversal during Retention Loss

To appropriately simulate the domain switching behaviors, critical polarization reversal parameters are calibrated from the experimental pulse measurements at different time durations and amplitudes (Fig. 3(a)). The kinetic Monte Carlo model (KMC) [7] is also implemented as a comparison, which predicts the switching event domain by domain. Both KMC and our PDE IFM models can properly capture the reversal dynamics. It should be noted that our PDE IFM model solves only one differential equation, with the local field variation in multi-domains parameterized by a deviation parameter σ. Therefore, our PDE IFM model is more computationally efficient compared to KMC (Fig. 3(b)), which is expected as a more promising scenario for implementations of large-scale circuit-level FTJ models.

A dynamic P-V hysteresis loop simulated by the IFM PDE model is shown in (Fig. 4(a)). Compared with an MFM structure, the remnant polarization P_r in MFIM is reduced due to the depolarization field. Such an effect can be significant, especially with small t_{FE} and large t_{IL}, leading to

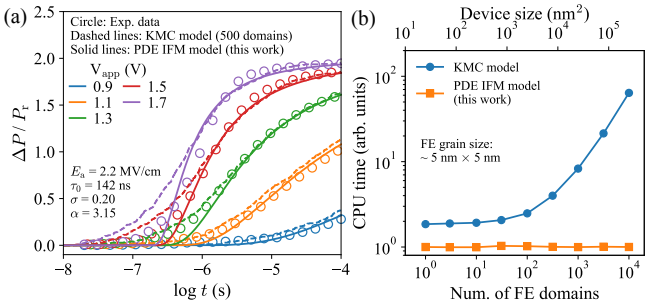

Fig. 3. (a) The experimentally measured polarization reversal dynamics can be properly calibrated by our PDE IFM model (solid lines) or KMC model (dashed lines) [7]. (b) PDE IFM model shows a superior computation efficiency especially as the number of FE domains increases.

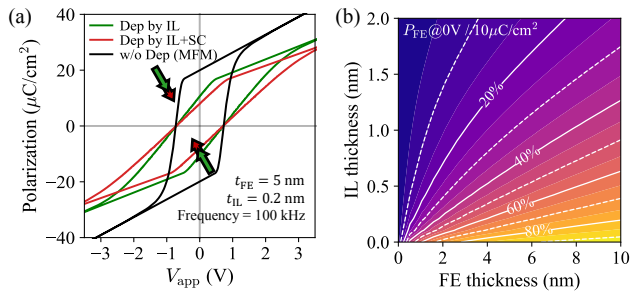

Fig. 4. (a) Dynamic $P-V$ hysteresis loop modulated by depolarization field, contributed from interfacial dead layer (IL) and/or finite screening charge in metal (SC). (b) Reduction of remnant polarization attributed to the depolarization effect with different FE and IL thicknesses. P_r =10 μC/cm^2.

~60% of P_r reduction with only 1 nm of t_{IL} (Fig. 4(b)). It is the main origin of the retention loss in the absence of external bias. Fig. 5 illustrates the temporal evolution of the remaining P_r and its retention loss rate. On a short timescale (e.g., $t < 1\ \mu s$), a high P_r magnitude gives rise to a large depolarization field, resulting in a fast relaxation process. However, on a much longer timescale $t \gg \tau_0$ (e.g., $t > 1$ ms), the retention loss rate dramatically decreases and converges. Then the remaining P_r is more sensitive to the percentile of inhomogeneous field distribution than its original P_r strength (Fig. 5(c)). According to the temporal evolution of P_r, a criterion with 50% remaining retention is used to identify the non-volatile/volatile property of an MFIM FTJ (Fig. 5(d)). Consequently, an ultra-thin IL is critical for a non-volatile FTJ, whereas thicker t_{IL} and thinner t_{FE} are beneficial to the volatile characteristics.

IV. Readout Current Characteristics of MFIM FTJ

The encoded information in FTJs is usually probed by a read current, with the tunnel barrier height modulated by ferroelectric polarization. In Fig. 6, the band diagrams at ON/OFF state regarding the low resistance ($+P_{FE}$) and high resistance ($-P_{FE}$) are calculated, including the modulation effects by SC and IF. The IF reduces the barrier area by rounding off the corners and suppressing the width and height. Such an effect becomes more substantial with a decreasing of layer thickness (Fig. 6(c)). Subsequently, we calculate the

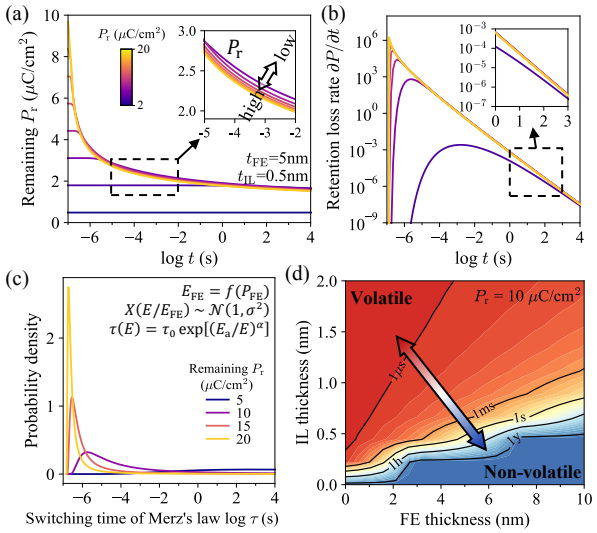

Fig. 5. (a) Polarization retention loss as a function of time, driven by depolarization field. (b) On a short timescale (e.g., $t < 1\ \mu s$), a high P_r has a fast retention loss rate due to a larger depolarization field. However, on a much longer timescale (e.g., $t > 1$ ms), the loss rate of different P_r converges. (c) Distribution of domain switching time τ. A broad distribution is attributed to the weak depolarization field by small P_r. (d) Polarization retention time until 50% P_r remains, which characterizes the non-volatile or volatile property.

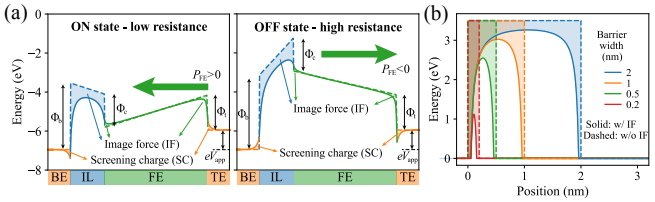

Fig. 6. (a) Band diagram for ON/OFF state of an MFIM FTJ. The trapezoidal potential (dashed lines) is modulated by polarization and applied voltage. Effect of image force and screening charge are illustrated (solid lines). (b) Barrier lowing effect by image force with different barrier width, which is more significant with a smaller layer thickness.

corresponding current-voltage relations of different polarization states (Fig. 7). To distinguish the contributions from the SC and IF, the ON/OFF-state current density at V_{Read} = 0.2 V is extracted (Fig. 8). Due to the barrier lowing effect by the IF, both J_{ON} and OFF-state current density (J_{OFF}) are raised ~3 times (with t_{FE} = 5 nm, t_{IL} = 0.5 nm). Opposite

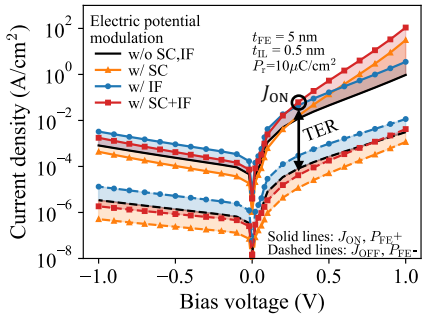

Fig. 7. Simulated current-voltage characteristics of MFIM FTJ based on default parameters. Dynamic polarization reversal is neglected.

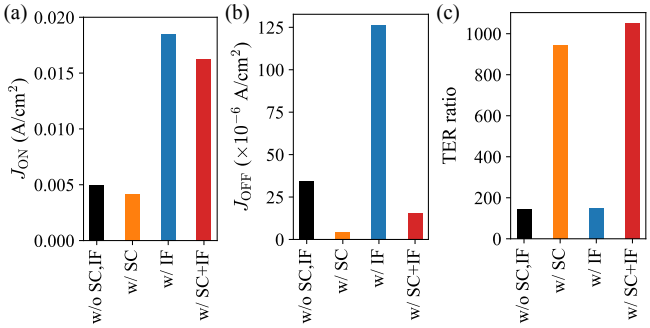

Fig. 8. Contributions by SC and IF modulation mechanisms on the ON/OFF-state read current. IF enhances both (a) J_{ON} and (b) J_{OFF}; SC mainly enhances (c) TER by significantly suppressing J_{OFF}. Tunneling current is extracted at V_{Read} = 0.2 V.

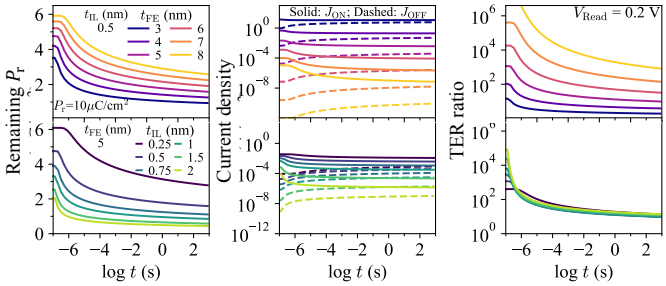

Fig. 9. Temporal evolution of polarization reversal (left column), ON/OFF-state current (middle column), and TER ratio (right column) during the retention loss process at $V_{\mathrm{app}} = 0$. Upper/lower rows indicates different t_{FE} or t_{IL}.

SC at top and bottom metals can enlarge the device asymmetry, giving rise to a great improvement in the TER ratio.

Fig. 9 shows variations of the J_{ON}, J_{OFF}, and TER ratio along with the polarization retention dynamics. As a result, J_{ON} follows the same trend as the remaining P_{r} decreases, accompanied by an increase in J_{OFF}. The combined effect leads to the reduction of the TER ratio by several orders of magnitude. Such a polarization retention loss causes severe performance degradation, with a slowdown of access speed (by $J_{\mathrm{ON}}\downarrow$) and a reduced read sensitivity (by TER$\downarrow$). Fortunately, by varying t_{FE} and t_{IL}, the magnitude and degradation rate of the J_{ON} and TER can be improved by several orders of magnitude. It indicates that a detailed study of the device design is necessary.

V. Design Space for Non-volatile/Volatile Applications

Herein, we investigate design spaces for non-volatile (Fig. 10) and volatile (Fig. 11) MFIM FTJs, respectively. A wide range of realistic material parameters are adopted to provide guidance for device fabrications (Fig. 10(a)). Concerning the non-volatile applications, sufficiently large J_{ON} and TER ratio are required over a long timescale (t = 10 s is adopted in this work). Compromised solutions for engineering FE and IL layers are shown in Figs. 10(b) and 10(c), as functions of the layer thickness t, dielectric constant ϵ, and electron affinity χ. As Hafnia-based ferroelectric materials have been widely employed, ±10% errors in $Hf_xZr_yO_2$ properties are examined. An enhancement of J_{ON} can be achieved by reducing the layer thickness (t_{FE} or t_{IL}) or tunnel barrier height (equivalent to large χ). However, a higher TER ratio is associated with a larger t_{FE}, which suggests a design of large t_{FE} with small t_{IL} can improve J_{ON} and TER simultaneously. Selections of top and bottom metal electrodes are investigated regarding their work functions Φ_{t} and Φ_{b} (Fig. 10(d)). Different work functions effectively raise a built-in field E_{BI}, which not only facilitates/mitigates the polarization retention loss, but also modulates the tunnel barriers. Essentially, decreasing both Φ_{t} and Φ_{b} is helpful for a large J_{ON}. By contrast, due to the asymmetry of the MFIM structure, the TER ratio can only be improved by smaller Φ_{t} and larger Φ_{b}.

For designing a volatile FTJ, the degradation of J_{ON} over time should be considered. In Figs. 11(a) and 11(b), among all the critical properties of FE and IL layers, t_{FE}, t_{IL} and ϵ_{IL} play major roles in the J_{ON} reduction. It should be noted that

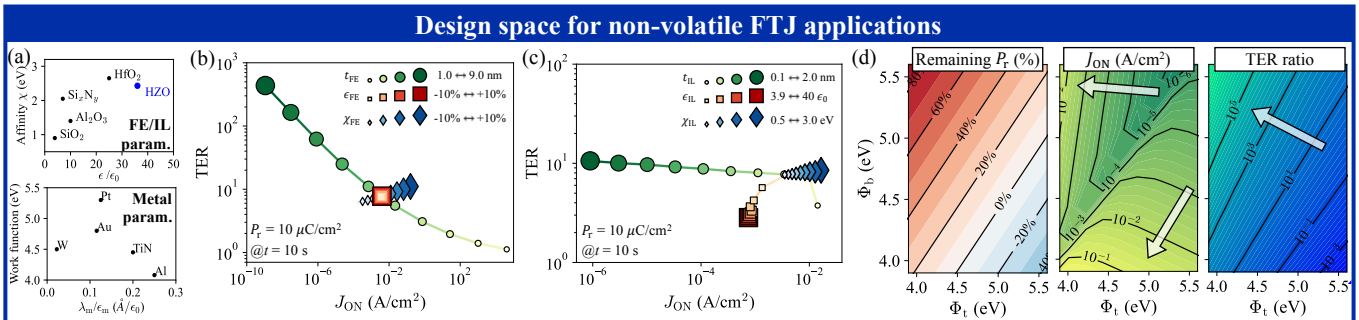

Fig. 10. (a) Range of material parameters considered in our simulations. (b)-(c) Influence of (b) FE layer and (c) IL layer property on tuning J_{ON} and TER. t_{FE} is varied, and ±10% errors on ϵ_{FE} and χ_{FE} are examined. t_{IL} and χ_{IL} play major roles on J_{ON}. ϵ_{IL} and χ_{IL} are varied based on (a). (d) Design space of the work function of metal electrodes on tuning J_{ON} and TER. Higher J_{ON} is obtained with small Φ_{t} or Φ_{b}, whereas improving TER ratio requires small Φ_{t} but large Φ_{b} (indicated by arrows).

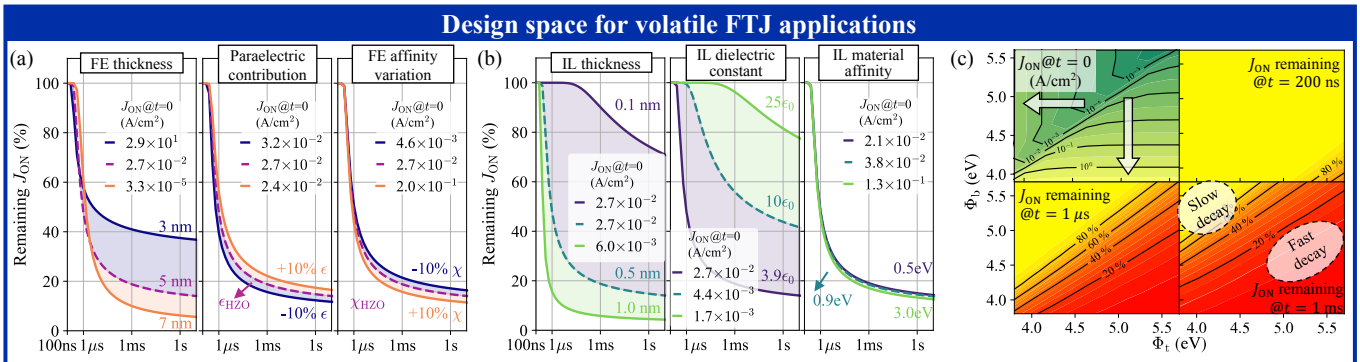

Fig. 11. Guideline for designing a volatile FTJ regarding the degradation of J_{ON} over time. (a)-(b) Within different (a) FE and (b) IL layer properties, the J_{ON} reduction rate mainly depends on t_{FE}, t_{IL} and ϵ_{IL}. ϵ_{FE}, χ_{FE}, and χ_{IL} have minor effects on J_{ON} reduction rate but induce significant variations on J_{ON} magnitude. $P_r = 10\ \mu C/cm^2$ is simulated and default parameters used for simulations are plotted with dashed lines. (c) Selection of the work function for metal electrodes. Design guideline of a large J_{ON} is the same as that of a non-volatile FTJ (Fig. 10). Fast J_{ON} decay rate is associated with small Φ_b but large Φ_t (dashed circles).

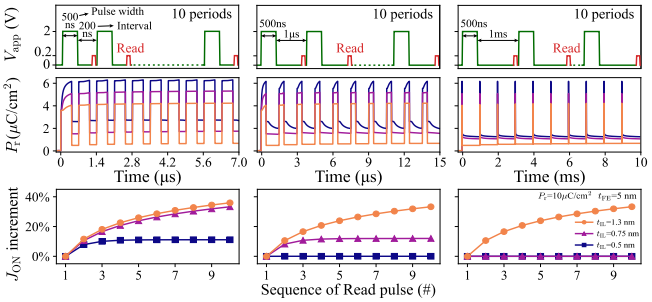

Fig. 12. Three volatile FTJ devices are designed with different degrees of dynamic response on ns/μs/ms timescales. An accumulation effect of J_{ON} is significant if a fast retention loss occurs, and short-interval (high-frequency) pulses are applied.

although ϵ_{FE}, χ_{FE}, and χ_{IL} have minor effects on the reduction rate, they can induce significant variations on the J_{ON} magnitude, which may act as potential causes of device-to-device variations to undermine the FTJ uniformity. Selection of electrode materials is also important (Fig. 11(c)). A basic guideline for the J_{ON} volatility is to increase Φ_t and decrease Φ_b coherently. Moreover, the dynamic response range is a technical indicator that is closely related to specific application scenarios. Inspired by the systematically explored design space, a set of volatile FTJs are designed with different sensitivities on ns/μs/ms timescales (Fig. 12). As a result, an accumulation effect of the read current can be acquired if the FTJ is more volatile (fast retention loss rate) and high-frequency pulses are applied. The robust and recognizable readout foresees great potential for upcoming applications by crafting volatile FTJs.

VI. Conclusion

We have developed a comprehensive MFIM FTJ model for dynamic polarization retention loss along with thorough considerations of the potential profile (Table. I). The dynamic module is highly efficient by parameterizing the inhomogeneity of a polycrystalline thin film into a single PDE. Dynamics of the polarization reversal on short and long timescales are determined by initial remnant polarization P_r and deviation of local field distribution σ, respectively. Image force and screening charge effects modulate the tunnel barrier, responsible for J_{ON} and TER ratio, respectively. Adopting small Φ_t and large Φ_b of electrode work functions can coherently enhance J_{ON} and TER ratio. In this work, the design spaces for performance optimization of MFIM FTJs are systematically studied, towards the guidance of their non-volatile and volatile applications.

	Wang et al. APL2014	Mo et al. IEDM2018	Huang et al. IEDM2019	Xiao et al. IEDM2021	Zhou et al. EDL2022	**This work**
FTJ type	MFM	MFIM+MFIS	MFIM	MFIS	MFIS	**MFIM**
FE reversal dynamics	KAI	Static Preisach	Static Preisach	Monte Carlo + NLS	TDLG	**PDE IFM**
Multi-domain characteristics	No	No	No	Yes	Yes	**Yes**
Potential profile calculation	Only App	App, Dep, SC, BI,	App, Dep	App, Dep	App, Dep, SC	**App, Dep, BI, SC, IF**
Tunneling current	WKB approx.	NEGF	WKB approx.	WKB approx.	NEGF	**WKB approx.**

*App: external applied voltage; Dep: depolarization field; BI: built-in field; SC: screening charge; IF: image force.

Table I. Comparisons of existing FTJ models. Our polarization reversal model is high-efficient, and especially appropriate for treating inhomogeneous local field in disordered materials, such as polycrystalline HZO thin films. The electrostatic potential profile is carefully considered towards realistic simulations of MFIM FTJs.

Acknowledgment

This work was supported by the National Key R&D Program of China under Grant No. 2022YFB3608400, the Strategic Priority Research Program of the Chinese Academy of Sciences under Grant No. XDB44000000, and MOE innovation platform.

References

[1] J. Y. Park *et al.*, "Revival of Ferroelectric Memories Based on Emerging Fluorite-Structured Ferroelectrics," *Adv. Mater.*, vol. 35, no. 43, p. 2204904, 2023.
[2] N. Zagni *et al.*, "Reliability of HfO_2-Based Ferroelectric FETs: A Critical Review of Current and Future Challenges," *Proc. IEEE*, vol. 111, no. 2, pp. 158-184, 2023.
[3] J. Yu *et al.*, "Energy Efficient and Robust Reservoir Computing System Using Ultrathin (3.5 nm) Ferroelectric Tunneling Junctions for Temporal Data Learning," *IEEE 2021 Symposium on VLSI Technology*.
[4] Z. Wang *et al.*, "Compact Modelling of Ferroelectric Tunnel Memristor and Its Use for Neuromorphic Simulation," *Appl. Phys. Lett.*, vol. 104, no. 5, p. 053505, 2014.
[5] F. Mo *et al.*, "Scalability Study on Ferroelectric-HfO_2 Tunnel Junction Memory Based on Non-equilibrium Green Function Method with Self-consistent Potential," *2018 IEEE International Electron Devices Meeting (IEDM)*, pp. 16.3.1-16.3.4.
[6] H.-H. Huang *et al.*, "A Comprehensive Modeling Framework for Ferroelectric Tunnel Junctions," *2019 IEEE International Electron Devices Meeting (IEDM)*, pp. 32.2.1-32.2.4.
[7] Y. Xiao *et al.*, "Predictive Modeling of Ferroelectric Tunnel Junctions for Memory and Analog Weight Cell Applications," *2021 IEEE International Electron Devices Meeting (IEDM)*, pp. 15.5.1-15.5.4.
[8] Z. Zhou *et al.*, "Time-Dependent Landau-Ginzburg Equation-Based Ferroelectric Tunnel Junction Modeling With Dynamic Response and Multi-Domain Characteristics," *IEEE Electron Device Lett.*, vol. 43, no. 1, pp. 158-161, 2022.
[9] S. Zhukov *et al.*, "Experimental and Theoretical Investigation on Polarization Reversal in Unfatigued Lead-Zirconate-Titanate Ceramic," *J. Appl. Phys.*, vol. 108, no. 1, p. 014106, 2010.
[10] J. G. Simmons, "Generalized Formula for the Electric Tunnel Effect between Similar Electrodes Separated by a Thin Insulating Film," *J. Appl. Phys.*, vol. 34, no. 6, pp. 1793–1803, 1963.
[11] M. Y. Zhuravlev *et al.*, "Giant Electroresistance in Ferroelectric Tunnel Junctions", *Phys. Rev. Lett.*, vol. 94, no. 24, p. 246802, 2005.